Decoupling and reprogramming the wiggling motion of midge larvae using a soft robotic platform

Neng Xia,[1§] Bowen Jin,[2§] Dongdong Jin,[1] Zhengxin Yang,[1] Chengfeng Pan,[1] Qianqian Wang,[1] Fengtong Ji,[1] Veronica Iacovacci,[1,3] Carmel Majidi,[4*] Yang Ding[2*] and Li Zhang[1,5,6,7*]

[1]Department of Mechanical and Automation Engineering, The Chinese University of Hong Kong, Hong Kong, China.
[2]Beijing Computational Science Research Center, Haidian District, Beijing, China.
[3]The BioRobotics Institute, Scuola Superiore Sant'Anna, Pisa 56025, Italy.
[4]Soft Machines Lab, Carnegie Mellon University, Pittsburgh, PA 15213, USA.
[5]Chow Yuk Ho Technology Center for Innovative Medicine, The Chinese University of Hong Kong, Hong Kong, China.
[6]CUHK T Stone Robotics Institute, The Chinese University of Hong Kong, Hong Kong, China.
[7]Department of Surgery, The Chinese University of Hong Kong, Hong Kong, China.
[§] Contribute equally to this work

*Correspondence to: Carmel Majidi, Yang Ding and Li Zhang
Email: cmajidi@andrew.cmu.edu, dingyang@csrc.ac.cn, lizhang@cuhk.edu.hk

Author Contributions: L. Z. and Y. D. conceptualized the research. N. X., D. J., and C. P. fabricated the soft robot. N. X. performed the magnetic actuation experiments and analyzed the experimental data. Z. Y. conducted the tracking and trajectory extraction of the robot. N. X. and D. J. performed the analysis of the motion of the robot. N. X. and Q. W. analyzed the fluid-structure interaction. F. J. performed the simulation for magnetic flux distribution. B. J. and Y. D. proposed the fluid dynamic simulation of the robot and analyzed the swimming mechanism of the robot. N. X., B. J., V. I., C. M., Y. D., and L. Z. wrote the paper. L. Z. and Y. D. supervised the research.
Competing Interest Statement: Authors declare that they have no competing interests.
Classification: Physical sciences; Engineering.
Keywords: motion decoupling, wiggling motion, magnetic robotic platform.

This PDF file includes:
Main Text
Figures 1 to 6
Table 1

Abstract

The efficient motility of invertebrates helps them survive under evolutionary pressures. Reconstructing the locomotion of invertebrates and decoupling the influence of individual basic motion are crucial for understanding their underlying mechanisms, which, however, generally remain a challenge due to the complexity of locomotion gaits. Herein, we develop a magnetic soft robot to reproduce midge larva's key natural swimming gaits and investigate the coupling effect

between body curling and rotation on motility. Through our systematically decoupling studies using programmed magnetic field inputs, the soft robot (named LarvaBot) experiences various coupled gaits, including biomimetic side-to-side flexures, and unveils that the optimal rotation amplitude and the synchronization of curling and rotation greatly enhance its motility. The LarvaBot achieves fast locomotion and upstream capability at the moderate Reynolds number regime. Our soft robotics-based platform provides new insight to decouple complex biological locomotion, and design programmed swimming gaits for the fast locomotion of soft-bodied swimmers.

Significance Statement

Natural organisms at different scales generally utilize the coupling of basic motions to yield efficient motility. Understanding the coupling effects of these biological gaits is crucial for grasping their underlying mechanisms and developing high-performance robots. Here, we present a magnetic soft robotic platform to decouple and reprogram complex wiggling motion adopted by invertebrates. By using a magnetic soft robot (named LarvaBot) and programmed magnetic field inputs, we unveil that the synchronization of body curling and rotation, and the optimal rotation amplitude greatly enhance the motility. Our robotic platform offers a new toolbox to decouple complex biological gaits and develop optimized soft-bodied swimmers with enhanced motility.

Main Text

Introduction

Natural organisms often exhibit high adaptability to complex environments due to the evolution of predator-prey interactions, such as ultrafast locomotion, camouflage, and group cooperation(1-3). Studies on natural motion and adaptation have significant influence on various engineering fields, ranging from bioinspired robotics to medical devices(4-10). However, given the complexity of biological behaviors, emulating and investigating these natural modes of locomotion with engineered systems has been challenging(11-13). In this respect, burgeoning effort has been devoted to developing new simulation tools, physical models, and experimental platforms. Among

these engineering tools, soft robotic systems are promising in light of their biologically-relevant mechanical compliance, deformability, and modes of locomotion(4, 14-17).

Untethered soft robots, which can freely move without requiring a physical connection to external hardware and power supplies, are especially good candidates for studying the locomotion modes of natural invertebrates(18-21). Thanks to recent advances in fabrication methods(22-26), functional materials(27-29), and actuation strategies(7, 30-35), roboticists have proposed several soft robots that are capable of mimicking some features of natural animal locomotion. For example, previous efforts with photo-responsive hydrogels-based robots demonstrated the ability to mimic peristaltic earthworm crawling(36). Likewise, untethered soft robots that are powered with shape memory alloy have been shown to exhibit a variety of locomotion modes, including undulation, jumping, crawling through narrow space or walking over rough terrain(37, 38). The application of magnetic soft robots in biomimetic study has received growing attention due to their high controllability. Hu *et al.* developed a millimeter-scale film robot that achieves multiple locomotion modes, e.g., jellyfish-like swimming and crawling(5). Recently, soft magnetic composites with programmable 3D magnetization and smart materials have been further developed to realize diverse biomimetic motorial capabilities(16, 22, 39, 40). However, despite such progress, many organisms at different scales exhibit more complex locomotion gaits that have been difficult to mimic with existing soft robotic platforms, and these platforms suffer from insufficiency of strategy to decouple the complex biological behaviors. This makes it challenging to reconstruct their locomotion behaviors or to understand the underlying mechanisms of the locomotion modes. For example, midge larvae (Chironomidae), swim rapidly (Reynolds number $Re \approx 465$) with a unique gait consisting of periodically curling into a circle shape coupled with body rotation and unfolding through muscle activation(41). The larvae yield faster swimming speed with a unique coupled gait (0.84 body length per motion cycle) compared with many other invertebrates (including nematode(42), polychaete worm(43), leech(44), caterpillar(45), and earthworm(46)) (*SI Appendix*, Table S1) and exhibit high adaptability to complex

environments(41). The study of the wiggling motion of midge larvae promises benefits in constructing soft aquatic robots with high mobility and adaptability, which is attractive to researchers.

In this work, we present a millimeter-scale magnetic soft robot (named LarvaBot) that reconstructs the natural swimming gait of midge larvae and provides a platform to understand their agile locomotion that could potentially guide actuation, gait selection, and path planning of other untethered swimming robots. The motion cycle of natural larvae is divided into two stages, and each of them consists of three types of gaits, including unfurling, curling, and rotation (Fig. 1*A*). LarvaBot is designed to achieve similar motion through the use of a shape programmable composite composed of soft hydrogel material doped with ferromagnetic particles with anisotropic magnetization. Taking advantage of photocurable hydrogel, we can facilely fabricate our soft robot (curing time less than 5 min) with a slender structure. Inspired by the morphology of midge larvae, we adopt a rod-shape structure which is different from the film-shape magnetic robots. New time-varying magnetic fields are introduced to induce the agile motion of our LarvaBot. A variety of reprogrammable coupled gaits, including the characteristic larvae ones, are created through our LarvaBot and programmed magnetic field inputs (Fig. 1*B*). By performing systematical decoupling studies, we unveil that the coupling of body curling and rotation plays a key role in its propulsion. In fact, we discover that an optimal rotation amplitude and the synchronization of curling and rotation greatly enhance its motility. Swimming with the biomimetic propulsion fashion can induce ring vortex structures consistent with the natural counterpart and achieve great motility (0.71 body length per motion cycle) at moderate Re regimes (1-2000)(47). Moreover, LarvaBot is capable of performing upstream locomotion in flowing fluid, adaptability to a three-dimensional (3D) environment by switching its locomotion modes, and other functionalities, including obstacle-crossing ability and movement in narrow space. This work provides a soft robotic platform allowing to decouple and reprogram the complex wiggling motion adopted by invertebrates and grasp their underlying mechanisms, and offers new insight for

designing optimized swimming soft robots with complex coupled gaits which may outperform their natural counterparts.

Results and discussion

Morphology and swimming gait of midge larvae. Chironomidae midge larvae, a kind of soft-bodied insect living in ponds, exhibit unique locomotion behavior(41). Fig. 1*A* illustrates a complete motion cycle and shape of the larvae. With a body length ranging from 2.0 to 29.4 mm, the larva consists of an anterior head, a slender body, and a posterior proleg(41, 48-50). The complex swimming gait of larva in the horizontal plane can be divided into two stages. At the beginning of the first half stroke, the larva's body flexes to one side and forming a circle-like structure, followed by body rotation and rapid unfurling. The larva body rotates approximately 180° after half-strokes. At the second stage, the larva coils to the other side, rotates along the opposite direction, and eventually points in almost the same direction as at the start(41, 51). An S-shaped trajectory can be obtained during one motion cycle and the direction of effective displacement generated by the asymmetric motion sequence is perpendicular to the larva body in the unfurling configuration. With the complex coupling of curling and rotation, the larvae can exhibit highly maneuverable swimming behavior that enable them to escape from many natural predators. Apart from fast swimming, multimodal locomotion including crawling, undulation, emersion, and immersion have been observed in larvae(41). This abundance of modalities in motile activity enables them to adapt to sophisticated physical environmental circumstances.

Reconstruction of the biomimetic locomotion. Inspired by the midge larvae, our LarvaBot exhibits slender structure and deformation to arc shape under external magnetic field. The comparison between the larvae and the LarvaBot is shown in Table 1. Considering the workspace of actuation setup and the morphological characteristics of the real larvae, the LarvaBot is designed as a slender rod structure whose length and aspect ratio are 5 mm and 11:1, respectively. The LarvaBot swims in an intermediate flow regime and the induced wake flow pattern is consistent

with the midge larvae (*Re* = 17-57). The difference in characteristic length of LarvaBot and collected larvae in reference (41) can lead to the difference in *Re* number. In this study, the robot body is composed of polyacrylamide (PAAm) hydrogel and hard magnetic NdFeB@SiO_2 particles (remanent magnetic moment: 85 emu/g, *SI Appendix*, Fig. S1) with an average diameter of 5 μm (*SI Appendix*, Fig. S2 and Fig. 2*A*). To avoid the sinking of the LarvaBot caused by gravity, hydrophobic treatment is conducted for the surface of the robot to enable stable locomotion at the air-water interface. Surface tension analysis in *SI Appendix*, section S1 demonstrates that the surface tension applied to the LarvaBot does not affect its locomotion. The shape transformation is controlled by the interaction between the magnetization of the robot and the programmed magnetic field. As shown in Fig. 2*A*, a template-assisted magnetization method is adopted to obtain a sinusoidal magnetization profile (***M*** **=** (m_x, m_y, 0)) inside the robot body. The magnetic flux density created by the magnetization profile of the LarvaBot is measured by a magneto-optical sensor (MagViewS, Matesy, Germany), as shown in Fig. 2*B*. A simulation for the sinusoidal magnetization profile is also developed on COMSOL (Fig. 2*B*). The good agreement between the simulation and measured results of surface magnetic flux density verifies the sinusoidal distribution of the magnetization profile.

The LarvaBot deforms into arc shapes with different curvatures and orientations by applying static magnetic fields, as shown in Fig. 2*C* and *SI Appendix*, Fig. S3. A 3-axis Helmholtz electromagnetic coil setup is employed to generate the magnetic field (*SI Appendix*, Fig. S4). The curvature of the deformed robot increases as the strength of the magnetic field increases. The deformation of the LarvaBot can be quantitatively described by the following elastic rod model(5):

$$\left(m_x sin\theta + m_y cos\theta\right)B_x - \left(m_x cos\theta - m_y sin\theta\right)B_y = \frac{EI}{A}\frac{\partial^2\theta}{\partial s^2} \quad (1)$$

Here E and θ represent the elastic modulus and the rotational deflection of the robot, respectively, I is the second moment of area of the robot, and A is the cross-sectional area of the robot. $\boldsymbol{B} = [B_x \quad B_y \quad B_z]^T$ represents the applied magnetic field. The calculated results of deformation are in

good agreement with the experimental results (Fig. 2*C*). The LarvaBot has a net magnetic moment $\boldsymbol{M}_{\text{net}}$ at rest and deformed states, which can be obtained by

$$\boldsymbol{M}_{net} = \int_L \boldsymbol{R_z} \boldsymbol{M} A \, ds \tag{2}$$

where *L* is the body length of the robot and $\boldsymbol{R_z}$ is a z-axis rotational matrix regarding the change in the direction of ***M*** *(5)*. As shown in Fig. 2*C*, the robot's $\boldsymbol{M}_{\text{net}}$ tends to be aligned with ***B***. When the direction of ***B*** changes suddenly, the LarvaBot undergoes rigid-body rotation or deformation depending on the magnitude of the change in the direction of ***B*** (*SI Appendix*, Fig. S5). When the angle exceeds 90°, the robot will be deformed until the $\boldsymbol{M}_{\text{net}}$ aligns with the direction of ***B***. In contrast, if the angle is less than 90°, a rigid-body rotation occurs.

Based on the magnetic responsive behaviors of the robot under the static magnetic field, a dynamic programmed magnetic field (*SI Appendix*, section S2) is designed to generate the larva-inspired swimming gait. We divide it into two parts to show the applied magnetic field more clearly, as shown in Fig. 2*D*. During the first half period, the magnetic field rotates with increasing strength until the magnitude reaches its maximum, and then it gradually decreases to 0 at a constant angle. During the second phase, the strength of the magnetic field changes with the same trend, but the magnetic field rotates in the opposite direction. The motion sequences of the LarvaBot induced by the proposed dynamic field are shown in Fig. 2*E*. During the CCW rotation period, the LarvaBot curls into arc shape and experiences rotation due to magnetic torque. At the end of the CCW rotation period, the robot body unfurls and points to the opposite direction compared with the initial orientation. Subsequently, the LarvaBot bends toward the other side and recoveries the same head-to-tail direction as at the beginning of the CW period. The motion sequences of the LarvaBot are consistent with the swimming gait of larvae shown in Fig. 1*A*. The net displacement over one cycle and swimming direction can be determined by the initial and final states of the LarvaBot. The swimming direction in Fig. 2*E* is approximately perpendicular to the robot's body at straightened

state. These results indicate that the proposed robot exhibits a consistent directional movement by emulating the swimming gait of larvae.

Swimming mechanism of the LarvaBot. The movement of the LarvaBot could be simplified into two key processes: unfurling of the robot body (unfurling process) and body rotation coupled with curling (C-R process). *SI Appendix*, Fig. S6 illustrates the variation of curvature and rotation angle of the LarvaBot during one motion cycle. The instantaneous velocity of the center of mass (COM) of the robot is shown in Fig. 3*A*. The positive displacement mainly occurs during the C-R process (blue regions in Fig. 3*A*). According to the movement trajectories extracted from experimental results, the rotation of the COM of the robot is observed. On the other hand, during the unfurling process, $\boldsymbol{M}_{\text{net}}$ aligns with the external magnetic field. However, no net magnetic torque and magnetic force act on the robot. Fluid dynamic simulation demonstrated that the fluid force acting on the robot is negligible. Therefore, the COM of the robot hardly changes (*SI Appendix*, Fig. S7). Based on the above analysis, the average velocity of the robot over one cycle could be calculated as

$$v = L_{C-R} \times f_{eq} = \frac{L_{C-R}}{\frac{1}{2f_1}\left(1+\frac{f_1}{f_2}\right)} \tag{3}$$

where $1/f_1$ and $1/f_2$ represent the duration of the C-R and unfurling process, respectively. f_{eq} is the frequency for one motion cycle. We define the net displacement generated during the C-R process as L_{C-R}.

Theoretical analysis is performed to study the fluid-structure interaction during the swimming process. We use a sine function to describe the variation of curvature of the robot body during one motion cycle. By performing computational fluid dynamic simulation with immersed boundary method (*SI Appendix*, section S3), the LarvaBot COM trajectory and the fluid-structure interaction can be derived. Fig. 3*B* shows the comparison between experimental and simulation results, in which the trajectory and shape of the robot over one cycle are included. The agreement between the experimental and simulation results validates the simulation model. The net fluid force acting

on the LarvaBot is shown in Fig. 3*C*. The net fluid force increases dramatically during the C-R process and becomes negligible during the unfurling process. This behavior is in line with the no net displacement of the LarvaBot COM during unfurling.

In addition, the impact of the biomimetic swimming gait on the flow field is studied. The wake structure created by the swimming gait is visualized using organic dye, as shown in Fig. 3*D* and Movie S1. As a result of motion generated by LarvaBot, an array of ring vortexes consisting of two counterrotating vortex cores is generated behind the robot, demonstrating that the propulsive force is derived by accelerating water into the wake structure. The vortex pattern is consistent with that induced by the motion of the larvae(51), which further verifies the biomimetic feature of the LarvaBot.

Further understanding the complex coupled wiggling motion using LarvaBot. Our LarvaBot-based platform provides an enabling robotic technology to decouple the influence of various kinematic parameters that significantly affect their swimming performance. Since providing a more accurate comparison of performance, we use the normalized velocity (v/fL, where v is the velocity of the robot, f is actuation frequency, L is the body length of the robot) to evaluate the motility of our LarvaBot(52). First, we study the coupling of the body curling and rotation by tuning the phase difference of these basic motions. The impact of the phase difference between curling and rotation on the motility and trajectory of the robot is shown in Fig. 4*A*, *SI Appendix*, Fig. S8, and Movie S2, where a minus value for phase difference means that there is a delay of rotation compared with the curling process. Experimental results illustrate that S-shaped trajectories are obtained under different phase differences. Moreover, the results show that performing the curling and rotation synchronously can yield the largest net displacement over one motion cycle rising to 769% when reaching the maximum. Furthermore, the impact of basic motion parameters (e.g., rotation amplitude, rotational speed, and deformation amplitude) on motility are investigated through the decoupling study on LarvaBot. As aforementioned, both LarvaBot and larvae rotate 180° after half-

strokes. Different rotation angles ranging from 0° to 360° are achieved by tuning the input magnetic field parameters. The 0° rotation angle indicates that the robot only experiences curling and unfurling. Fig. 4*B* and *SI Appendix*, Fig. S9 show that the motility (*v*/*fL*) of LarvaBot attains its maximum at 180° rotation with a rise of 1245%. This confirms that the optimal ability of the proposed microrobot is consistent with the biological larva behavior reported in previous work(41). In addition, we analyzed the variation of deformation amplitude by tuning the magnetic field strength. With the increase of the magnitude of ***B***, the curvature of the deformed robot also increases (*SI Appendix*, Fig. S10), and the results show a rise by 82% in motility when reaching the peak velocity (Fig. 4*C*). The fluctuation amplitude of the motility caused by the change of the magnetic field strength is smaller than those caused by the variation of phase difference and rotation amplitude.

The impacts of the duration of C-R (curling and rotation) and unfurling processes are studied through the variations of their relative frequencies f_2/f_1 and total frequency f_{eq} of the full motion cycle. Fig. 4*D* shows the effect of f_2/f_1 on motility (when fixing f_{eq} = 1 Hz). The normalized velocity *v*/*fL* reaches its maximum when f_2/f_1 = 0.67, which indicates the propulsion efficiency benefits from comparable C-R and unfurling processes duration. Furthermore, f_{eq} also has an effect on the motility, as shown in Fig. 4*E* (where f_2/f_1 is fixed at 1). *v*/*fL* reaches its maximum (0.71 body length per cycle) when f_{eq} increases up to 2 Hz and drops to 0.26 body length per cycle at f_{eq} = 3.5 Hz. This demonstrates that the performance of the LarvaBot also relies on its actuation frequency.

LarvaBot is capable of executing a natural swimming gait with controllable propulsion that is optimized for speed. As shown in Fig. 4*F*, there is a linear relationship between the moving direction of the LarvaBot and the direction angle of the magnetic field (R^2 = 0.99). When employing optimized magnetic field parameters, LarvaBot outperforms most reported robots at moderate *Re* regime in terms of motility/body weight ratio (Fig. 5)(5, 41, 53-57). Compared with the film robot with jellyfish-like swimming(5), the LarvaBot breaks time-reversal symmetry and generates an S-shaped trajectory (Fig. 3*B*) within one motion cycle. With a weight of only 0.797 mg, the LarvaBot owns fast

forward speed (0.71 body length per cycle). Nevertheless, LarvaBot velocity is still lower than the biological counterpart(41) (0.84 body length per cycle at 2.66 Hz). The discrepancy of motility between the proposed LarvaBot and larvae can be attributed to the difference in surface friction caused by the material.

Multimodal locomotion of the LarvaBot. Controllability and robustness are potentially important features in the design and operation of soft robots. Taking advantage of the larva-inspired swimming gait, we demonstrate a trajectory control for the LarvaBot, as shown in Fig. 6*A* and Movie S3. The LarvaBot could complete a pentagram-shaped trajectory by tuning the direction angle of the magnetic field, which demonstrates the controllability of the swimming gait. Furthermore, the robustness of the LarvaBot is verified in the flowing condition generated by a peristaltic pump. As shown in Fig. 6*B* and Movie S4, the robot is passively carried by the flowing fluid with an average speed of 5.5 mm/s when the magnetic field is off. By applying the magnetic field in Fig. 2*D* (f_{eq} = 3 Hz), the LarvaBot could swim against the drag force of the flowing water.

Apart from the swimming gait mentioned above, the larvae also show multimodal locomotion to accommodate various physical environmental circumstances and in response to threats. The transformable locomotion modes are achieved by different patterns of muscle activation. Inspired by these behaviors of larvae, various time-varying magnetic fields are designed to generate series of locomotion modes. As shown in Fig. 6*C*, the LarvaBot swims along a 3D trajectory by tuning the pitch angle of the magnetic field (*SI Appendix*, section S2 and *SI Appendix*, Fig. S11). To demonstrate the controllability of the 3D swimming behavior, the LarvaBot is manipulated to pass through a ring-shaped obstacle back and forth many times (Movie S5). In addition, the slender body of the robot enables it to go through a small size tube easily. As shown in Fig. 6*D* and Movie S6, thanks to the precise control using the applied magnetic field, the robot can enter a tube with a 1.8 mm inner diameter from an open environment and move crawl inside the tube. Untethered robots that could move in a narrow space have broad application prospects, such as executing detection

in harsh environments and carrying drugs for treatment in blood vessels. Unlike film-shaped robots, the proposed slender robot with circular cross-section exhibits more flexible motion and suffers from fewer space restrictions, making it more suitable for accomplishing tasks in narrow spaces.

Furthermore, a sequential series of locomotion modes can be performed by the LarvaBot in order to allow it to move in 3D space. As shown in Fig. 6*E* and Movie S7, the LarvaBot initially swims at the air-water interface with the bioinspired swimming gait. Just as natural larvae can escape from a liquid surface when they receive external stimuli, our robot can also emerge from water and quickly climb a stair by rolling. Subsequently, the LarvaBot swims over a standing obstacle as high as 8 mm (1.6 body length), demonstrating its obstacle crossing ability. *SI Appendix*, Fig. S12 and Movie S8 summarize seven different locomotion modes achieved by the robot. The multimodal locomotion capability makes the robot promising to study the biomechanics of other organisms (such as leech and earthworm) and perform functional tasks in harsh environments.

Conclusion

In summary, we create a soft robotics-based platform to reconstruct and decouple the complex wiggling motion adopted by midge larvae. The LarvaBot with slender structure can be fabricated by the photopolymerization of magnetic hydrogel material. Through the wireless actuation of programmed magnetic field inputs, the LarvaBot achieves a variety of reprogrammable coupled gaits, including motions that mimic natural larvae locomotion. Furthermore, such a robotic platform provides an enabling technology to systematically decouple the complex wiggling motion generated by larvae and provides insight into how rotation amplitude and the synchronization of curling and rotation can influence propulsion performance. We expect this study could assist in decoupling complex gaits generated by invertebrates and lead to a deeper understanding of their underlying mechanisms. Moreover, it can inform the design and operation of future miniaturized soft robots with programmed swimming gaits that are optimized for enhanced motility.

Materials and Methods

Materials

The chemicals of acrylamide (AAm, 99%), polyvinylpyrrolidone (PVP, average M_w ~ 1300000), glycerol, sodium chloride (NaCl, 99.5%), triethoxy-1H, 1H, 2H, 2H-tridecafluoro-n-octylsilane ($C_{14}H_{19}F_{13}O_3Si$, 97%), methylene blue (90.0%) and ammonia solution (25-28%) were obtained from Aladdin Chemicals. *N*,*N'*-methylene bisacrylamide (MBA) was purchased from Beijing Solarbio Science & Technology Co., Ltd. Diphenyl(2,4,6-trimethylbenzoyl)phosphine oxide (TPO-L) was purchased from Shanghai Curease Chemical Co., Ltd. Tetraethylorthosilicate (TEOS) was purchased from J&K Scientific Ltd. NdFeB microparticles with an average size of 5 μm (LW-BA(16-7A)-2000) were purchased from Guangzhou Xinnuode Co., Ltd. All chemicals were used without further purification.

Preparation of PAAm hydrogel precursor

First, 2g AAm, 0.01g BIS and 1g PVP were added to 10 mL deionized water and glycerol mixed solution (mass ratio: 1:1) and then stirred vigorously. After complete dissolution, 200 μL TPO-L/ethanol solution (10 wt.%) were mixed, followed by stirring for 10 min.

Preparation of NdFeB@SiO_2 particles

The silica shell of the NdFeB particle was obtained by the hydrolysis and polycondensation of TEOS. First, 18 g NdFeB particles were dispersed in 450 ml ethanol with vigorously stirring, followed by the addition of 27 ml ammonium hydroxide. 1.2 ml TEOS was then slowly added to the mixture. Subsequently, the mixture was stirred for 12 hours.

Magnetization procedure

The internal magnetic domain is programmed by template-assisted magnetization, as shown in Fig. 2*A*. The proposed soft robot is deformed by a rod mold and exposed to a uniform ~2 T magnetic field produced by a magnetizer. After magnetization, there is a sinusoidal magnetization profile (***M***) inside the robot body.

Magnetic Actuation Experiments

The soft robot was treated with 1 vol% Triethoxy-1H, 1H, 2H, 2H-tridecafluoro-n-octylsilane in ethanol to obtain a hydrophobic surface. This treatment could ensure that the robot stably stays on the water surface. A 3-axis Helmholtz electromagnetic coil setup was adopted to generate a programmable magnetic field. The proposed dynamic magnetic fields were controlled by custom-programmed software using LabVIEW.

Characterization Techniques

The magnetization profile of the soft robot was measured by a magneto-optical sensor (MagViewS, Matesy, Jena, Germany). The magnetic hysteresis of magnetic particles was measured by a PPMS Model 6000 Quantum Design VSM.

Acknowledgments

The research work is financially supported by the Hong Kong Research Grants Council with project No. JLFS/E-402/18, the ITF project with Project No. MRP/036/18X funded by the HKSAR Innovation and Technology Commission (ITC), the Croucher Foundation Grant with Ref. No. CAS20403, the CUHK internal grants, and National Science Foundation of China (NSFC-NSAF Grant No. U1930402). We thank the support from Multi-scale Medical Robotics Centre (MRC), InnoHK, at the Hong Kong Science Park. V.I. acknowledges funding from the European Union's Horizon 2020 research and innovation programme under the Marie Sklodowska-Curie grant agreement No. 894425.

References

1. M. Burrows, M. Dorosenko, Rapid swimming and escape movements in the aquatic larvae and pupae of the phantom midge Chaoborus crystallinus. *J. Exp. Biol.* **217**, 2468-2479 (2014).
2. Y. Ozkan-Aydin, D. I. Goldman, M. S. Bhamla, Collective dynamics in entangled worm and robot blobs. *Proc. Natl Acad. Sci.* **118**, e2010542118 (2021).
3. M. Qin *et al.*, Bioinspired hydrogel interferometer for adaptive coloration and chemical sensing. *Adv. Mater.* **30**, 1800468 (2018).
4. Z. Ren, W. Hu, X. Dong, M. Sitti, Multi-functional soft-bodied jellyfish-like swimming. *Nat. Commun.* **10**, 1-12 (2019).

5. W. Hu, G. Z. Lum, M. Mastrangeli, M. Sitti, Small-scale soft-bodied robot with multimodal locomotion. *Nature* **554**, 81-85 (2018).
6. Y. Tang *et al.*, Leveraging elastic instabilities for amplified performance: Spine-inspired high-speed and high-force soft robots. *Sci. Adv.* **6**, eaaz6912 (2020).
7. Y. Ohm *et al.*, An electrically conductive silver–polyacrylamide–alginate hydrogel composite for soft electronics. *Nat. Electron.* **4**, 185-192 (2021).
8. X. Liu *et al.*, Ingestible hydrogel device. *Nat. Commun.* **10**, 1-10 (2019).
9. M. Cianchetti, C. Laschi, A. Menciassi, P. Dario, Biomedical applications of soft robotics. *Nat. Rev. Mater.* **3**, 143-153 (2018).
10. Y. Wang *et al.*, A biorobotic adhesive disc for underwater hitchhiking inspired by the remora suckerfish. *Sci. Robot.* **2**, eaan8072 (2017).
11. J. M. Rieser, J. L. Tingle, D. I. Goldman, J. R. Mendelson, Functional consequences of convergently evolved microscopic skin features on snake locomotion. *Proc. Natl Acad. Sci.* **118** (2021).
12. J. A. Nyakatura *et al.*, Reverse-engineering the locomotion of a stem amniote. *Nature* **565**, 351-355 (2019).
13. A. J. Ijspeert, Biorobotics: Using robots to emulate and investigate agile locomotion. *Science* **346**, 196-203 (2014).
14. H. Gu *et al.*, Magnetic cilia carpets with programmable metachronal waves. *Nat. Commun.* **11**, 1-10 (2020).
15. X. Dong *et al.*, Bioinspired cilia arrays with programmable nonreciprocal motion and metachronal coordination. *Sci. Adv.* **6**, eabc9323 (2020).
16. T. Wang, Z. Ren, W. Hu, M. Li, M. Sitti, Effect of body stiffness distribution on larval fish–like efficient undulatory swimming. *Sci. Adv.* **7**, eabf7364 (2021).
17. D. Krishnamurthy, G. Katsikis, A. Bhargava, M. Prakash, Schistosoma mansoni cercariae swim efficiently by exploiting an elastohydrodynamic coupling. *Nat. Phys.* **13**, 266-271 (2017).
18. B. Wang, K. Kostarelos, B. J. Nelson, L. Zhang, Trends in Micro‐/Nanorobotics: Materials Development, Actuation, Localization, and System Integration for Biomedical Applications. *Adv. Mater.* **33**, 2002047 (2020).
19. E. W. Hawkes, C. Majidi, M. T. Tolley, Hard questions for soft robotics. *Sci. Robot.* **6**, eabg6049 (2021).
20. D. S. Shah *et al.*, A soft robot that adapts to environments through shape change. *Nat. Mach. Intell.* **3**, 51-59 (2021).
21. D. Shah *et al.*, Shape changing robots: Bioinspiration, simulation, and physical realization. *Adv. Mater.* **33**, 2002882 (2021).
22. Y. Kim, H. Yuk, R. Zhao, S. A. Chester, X. Zhao, Printing ferromagnetic domains for untethered fast-transforming soft materials. *Nature* **558**, 274-279 (2018).
23. J. Cui *et al.*, Nanomagnetic encoding of shape-morphing micromachines. *Nature* **575**, 164-168 (2019).
24. Y. Kim, G. A. Parada, S. Liu, X. Zhao, Ferromagnetic soft continuum robots. *Sci. Robot.* **4**, eaax7329 (2019).
25. X. Hu *et al.*, Magnetic soft micromachines made of linked microactuator networks. *Sci. Adv.* **7**, eabe8436 (2021).
26. J. Zhang *et al.*, Voxelated three-dimensional miniature magnetic soft machines via multimaterial heterogeneous assembly. *Sci. Robot.* **6**, eabf0112 (2021).

27. D. Jin *et al.*, Four-dimensional direct laser writing of reconfigurable compound micromachines. *Mater. Today.* **32**, 19-25 (2020).
28. Y. Zhao *et al.*, Somatosensory actuator based on stretchable conductive photothermally responsive hydrogel. *Sci. Robot.* **6**, eabd5483 (2021).
29. X. Liu *et al.*, Magnetic Living Hydrogels for Intestinal Localization, Retention, and Diagnosis. *Adv. Funct. Mater.* **31**, 2010918 (2021).
30. J. Yu, B. Wang, X. Du, Q. Wang, L. Zhang, Ultra-extensible ribbon-like magnetic microswarm. *Nat. Commun.* **9**, 1-9 (2018).
31. Q. Wang *et al.*, Ultrasound Doppler-guided real-time navigation of a magnetic microswarm for active endovascular delivery. *Sci. Adv.* **7**, eabe5914 (2021).
32. B. Wang *et al.*, Endoscopy-assisted magnetic navigation of biohybrid soft microrobots with rapid endoluminal delivery and imaging. *Sci. Robot.* **6**, eabd2813 (2021).
33. X. Qian *et al.*, Artificial phototropism for omnidirectional tracking and harvesting of light. *Nat. Nanotechnol.* **14**, 1048-1055 (2019).
34. D. Ahmed *et al.*, Neutrophil-inspired propulsion in a combined acoustic and magnetic field. *Nat. Commun.* **8**, 1-8 (2017).
35. Z. Ren *et al.*, Soft-bodied adaptive multimodal locomotion strategies in fluid-filled confined spaces. *Sci. Adv.* **7**, eabh2022 (2021).
36. Z. Sun *et al.*, An Anisotropic Hydrogel Actuator Enabling Earthworm‐Like Directed Peristaltic Crawling. *Angew. Chem., Int. Ed.* **57**, 15772-15776 (2018).
37. X. Huang *et al.*, Chasing biomimetic locomotion speeds: Creating untethered soft robots with shape memory alloy actuators. *Sci. Robot.* **3**, eaau7557 (2018).
38. S. Chen *et al.*, Soft crawling robots: design, actuation, and locomotion. *Adv. Mater. Technol.* **5**, 1900837 (2020).
39. T. Xu, J. Zhang, M. Salehizadeh, O. Onaizah, E. Diller, Millimeter-scale flexible robots with programmable three-dimensional magnetization and motions. *Sci. Robot.* **4**, eaav4494 (2019).
40. H. Lu *et al.*, A bioinspired multilegged soft millirobot that functions in both dry and wet conditions. *Nat. Commun.* **9**, 1-7 (2018).
41. J. Brackenbury, Locomotory modes in the larva and pupa of Chironomus plumosus (Diptera, Chironomidae). *J. Insect Physiol.* **46**, 1517-1527 (2000).
42. S. Park *et al.*, Enhanced Caenorhabditis elegans locomotion in a structured microfluidic environment. *PloS one* **3**, e2550 (2008).
43. R. A. Merz, D. R. Edwards, Jointed setae–their role in locomotion and gait transitions in polychaete worms. *J. Exp. Mar. Bio. Ecol.* **228**, 273-290 (1998).
44. J. Chen, W. Friesen, T. Iwasaki, Mechanisms underlying rhythmic locomotion: body–fluid interaction in undulatory swimming. *J. Exp. Biol.* **214**, 561-574 (2011).
45. J. Brackenbury, Fast locomotion in caterpillars. *J. Insect Physiol.* **45**, 525-533 (1999).
46. K. J. Quillin, Kinematic scaling of locomotion by hydrostatic animals: ontogeny of peristaltic crawling by the earthworm lumbricus terrestris. *J. Exp. Biol.* **202**, 661-674 (1999).
47. C. J. Voesenek, F. T. Muijres, J. L. Van Leeuwen, Biomechanics of swimming in developing larval fish. *J. Exp. Biol.* **221**, jeb149583 (2018).
48. T. J. Anderson, R. S. Stelzer, H. G. Drecktrah, S. L. Eggert, Secondary production of Chironomidae in a large eutrophic lake: implications for lake sturgeon production. *Freshw. Sci.* **31**, 365-378 (2012).

49. A. Roskosch, M. R. Morad, A. Khalili, J. Lewandowski, Bioirrigation by Chironomus plumosus: advective flow investigated by particle image velocimetry. *J. N. Am. Benthol. Soc* **29**, 789-802 (2010).
50. R. Cornette *et al.*, Chironomid midges (Diptera, Chironomidae) show extremely small genome sizes. *Zool. Sci.* **32**, 248-254 (2015).
51. J. Brackenbury, Swimming kinematics and wake elements in a worm-like insect: the larva of the midge Chironomus plumosus (Diptera). *J. Zool.* **260**, 195-201 (2003).
52. H.-W. Huang *et al.*, Adaptive locomotion of artificial microswimmers. *Sci. Adv.* **5**, eaau1532 (2019).
53. J. Zhang, E. Diller, Untethered miniature soft robots: Modeling and design of a millimeter-scale swimming magnetic sheet. *Soft Robot.* **5**, 761-776 (2018).
54. S. Wu *et al.*, Symmetry-Breaking Actuation Mechanism for Soft Robotics and Active Metamaterials. *ACS Appl. Mater. Interfaces* **11**, 41649-41658 (2019).
55. Y. Zhao *et al.*, Soft phototactic swimmer based on self-sustained hydrogel oscillator. *Sci. Robot.* **4**, eaax7112 (2019).
56. S. A. Budick, D. M. O'Malley, Locomotor repertoire of the larval zebrafish: swimming, turning and prey capture. *J. Exp. Biol.* **203**, 2565-2579 (2000).
57. L. A. Smock, Relationships between body size and biomass of aquatic insects. *Freshw. Biol.* **10**, 375-383 (1980).

Figures and Tables

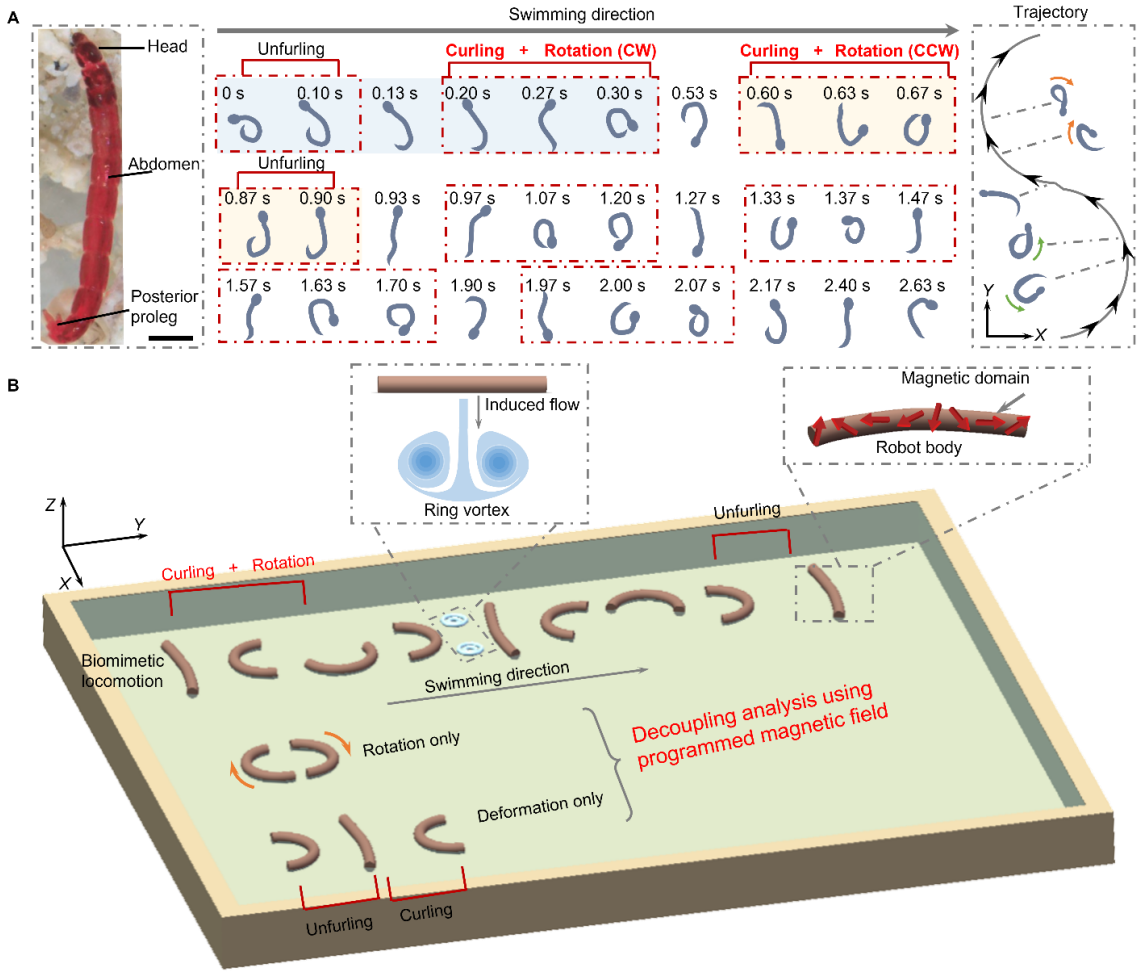

Figure 1. Schematics of the larvae and lavabot locomotion. (*A*) Image and swimming behavior of midge larva in the horizontal plane. Red boxes are used to indicate critical postures of the larva. The motion of larva can be divided into two stages, each consisting of unfurling and coupled curling and rotation. Larva coils to different sides in the two stages. CW and CCW represent clockwise and counterclockwise rotation, respectively. A schematic diagram of the trajectory of larva is shown on the right side of the graph. An S-shaped trajectory is generated during the swimming behavior and the inset images of larva show their orientations. The photo of larva is reproduced from(50). The gaits are extracted from the motion of real midge larvae. Scale bar is 1 mm. (*B*) Schematics of the LarvaBot with a variety of reprogrammable coupled gaits including the biomimetic swimming gait and the decoupling of basic motion. The basic gaits of the robot include curling, unfurling, and rotation, which are activated by a time-varying magnetic field. A ring vortex structure is generated by the propulsion of the LarvaBot and consistent with the wake structure created by the larvae.

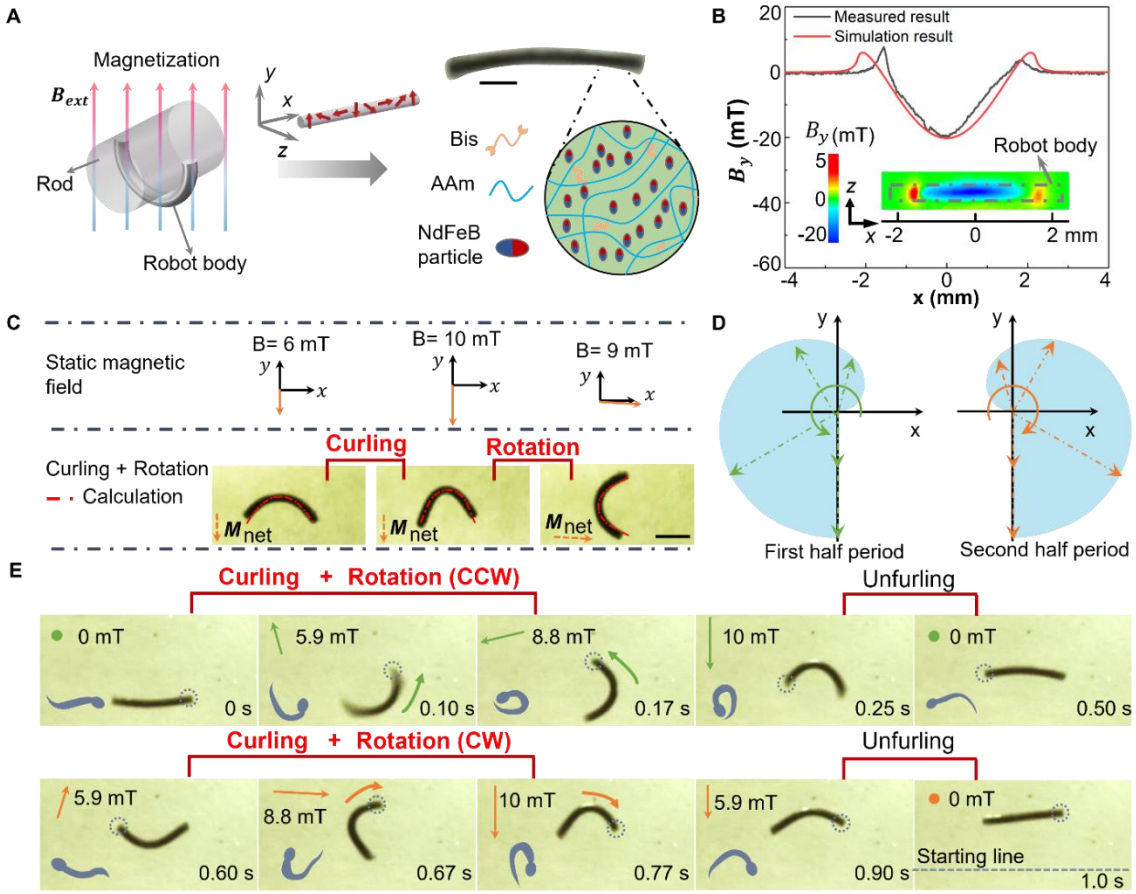

Figure 2. Magnetic control and motion analysis of the LarvaBot. (*A*) Magnetization of the robot. The scale bar is 1 mm. (*B*) Simulation and measured results of magnetic flux density distribution (B_y) along the centerline of the LarvaBot. The inset shows magnetic flux density distribution at the robot surface measured by a magneto-optical sensor. (*C*) Deformation and orientation of the LarvaBot under different static magnetic fields. The scale bar is 2 mm. (*D*) Magnetic field used to control the swimming behavior of LarvaBot. The straight arrows represent the time-varying magnetic field. The magnetic field rotates clockwise (CW) and counterclockwise (CCW) represented by the green and orange colors, respectively. During the first half period, the magnetic field rotates with increasing strength until the magnitude reaches its maximum, and then it gradually decreases to 0 at a constant angle. During the second period, the strength of the magnetic field changes in the same trend, but the magnetic field rotates in the opposite direction. (*E*) Motion sequence of the LarvaBot in one cycle. The scale bar is 2 mm. The dashed circles indicate the 'head' of the robot and distinguish the orientation of the robot body at different times.

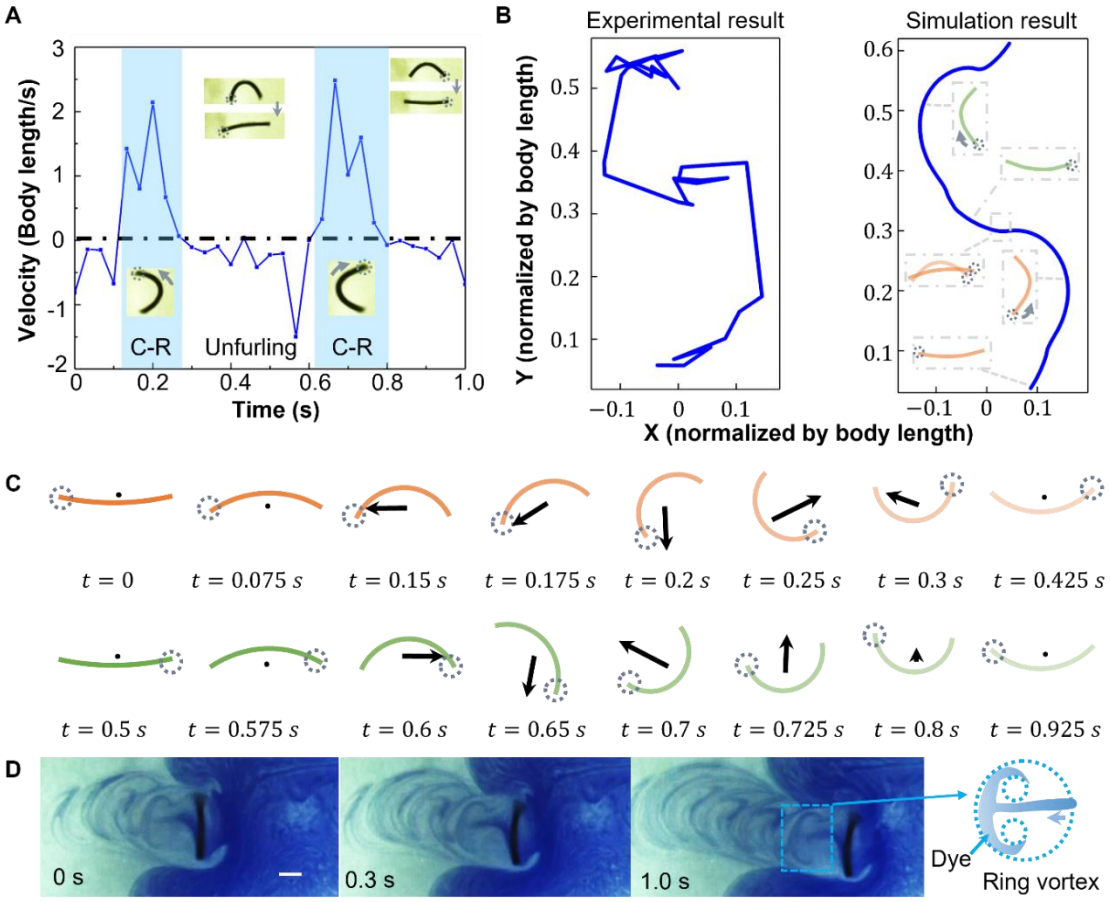

Figure 3. Fluid dynamic simulation and visualization of wake structure. (*A*) Measured instantaneous velocity of the LarvaBot in one cycle. The inset images show the robot during the unfurling process and C-R process. (*B*) Experimental and simulation results for the trajectory of the center of mass (COM) of the LarvaBot. The inset schematics show the orientation of the robot at different positions. The displacement of the robot in *X* and *Y* direction is normalized by its body length. (*C*) Net fluid force applied to the robot body over one motion cycle. Green and orange curves represent the orientation of the robot at different times, and black arrows represent the direction and amplitude of net fluid force. (*D*) Wake structure visualized by dye and geometry of ring vortex. The scale bar is 2 mm.

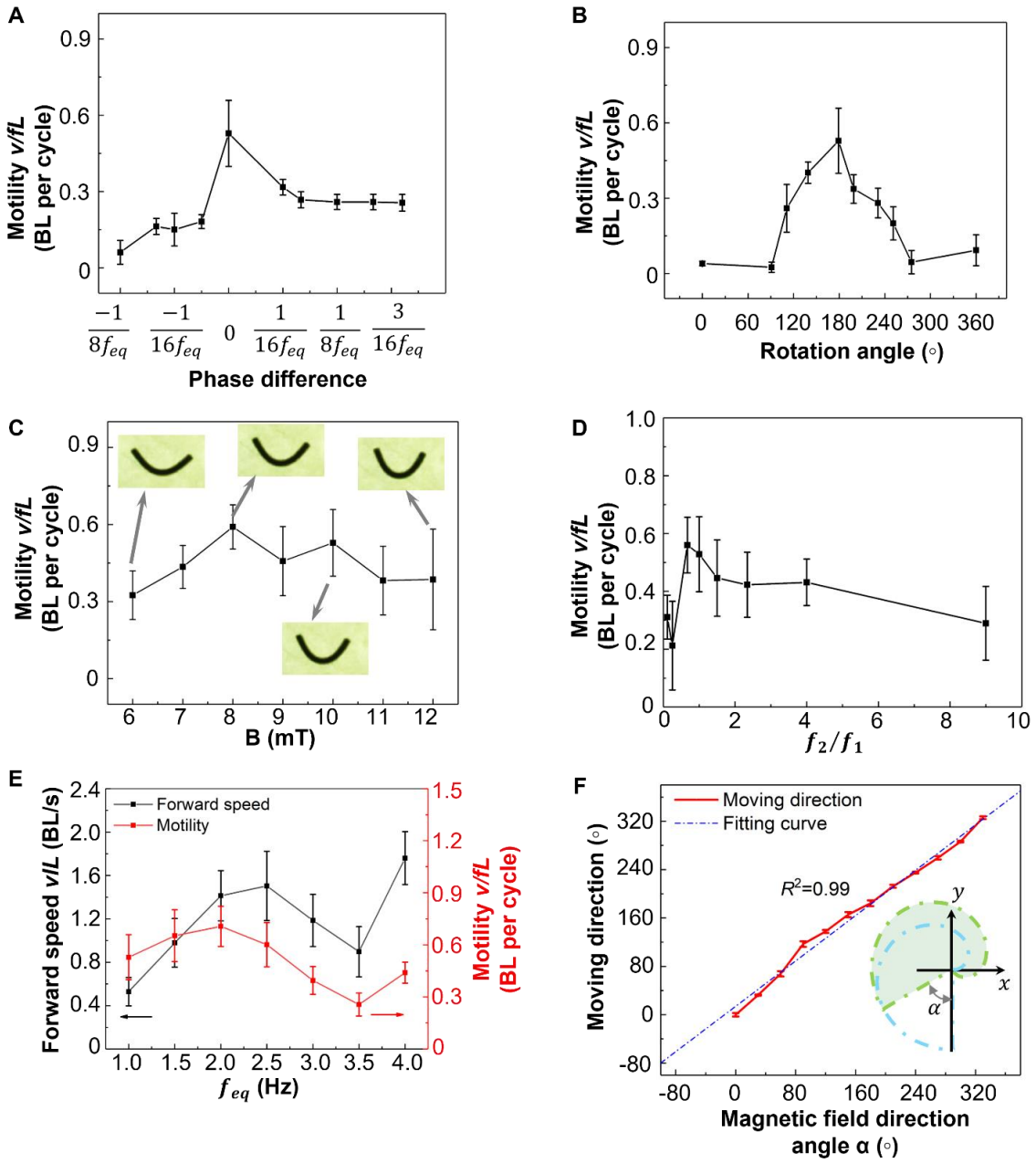

Figure 4. LarvaBot-based platform for decoupling the complex wiggling motion. (*A*) Effect of the phase difference between curling and rotation on motility. The minus value represents that there is a phase lag of rotation compared with the curling process. BL represents body length of the LarvaBot. (*B*) Effect of the rotation angle of robot body over half cycle on the motility. (*C*) Effect of magnetic field strength on the motility of the LarvaBot. Inset images show the deformation of the LarvaBot under B = 6, 8, 10, and 12 mT. (*D*) Effect of f_2/f_1 on the motility of the LarvaBot. (*E*) Effect of f_{eq} on the motility and forward velocity (BL/s) of the LarvaBot. (*F*) Relationship between moving direction and the direction angle of the magnetic field. The inset image shows the definition of the direction angle of the magnetic field. To describe the moving direction of the LarvaBot, we use the swimming direction of the robot under the direction angle of 0◦ as a baseline

for comparison. Error bars represent the standard error of the mean and the number of trials n = 6.

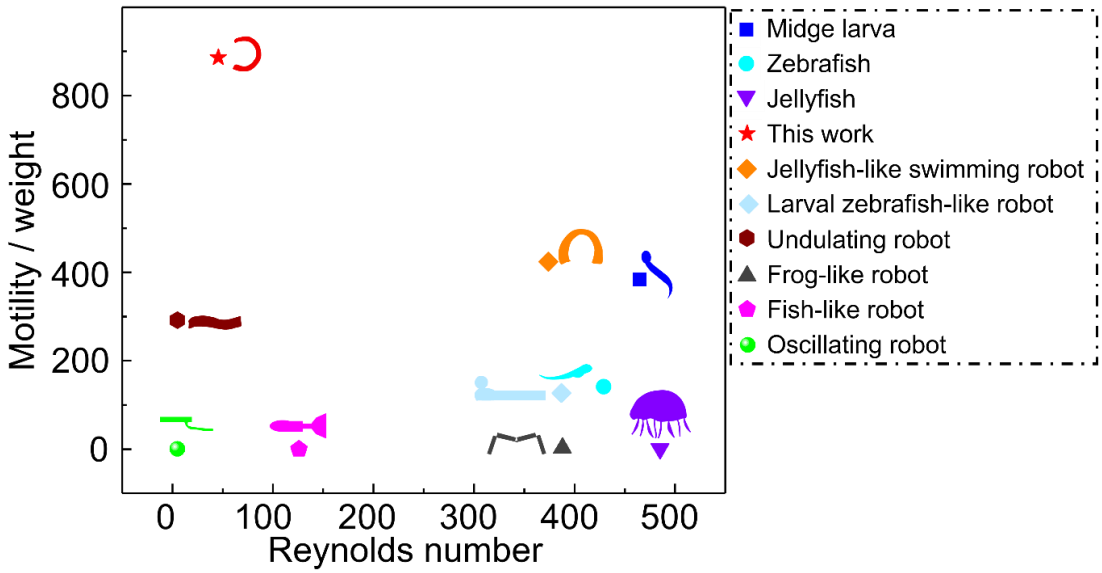

Figure 5. Comparison between LarvaBot, other swimming soft robots and invertebrates at moderate *Re* regime presented in the literature. Other swimming soft robots include jellyfish-like swimming robot(5), undulating robot(53), larval zebrafish-like robot(16), frog-like robot(54), and oscillating robot(55), and organisms include midge larvae(41, 57) and zebrafish(56).

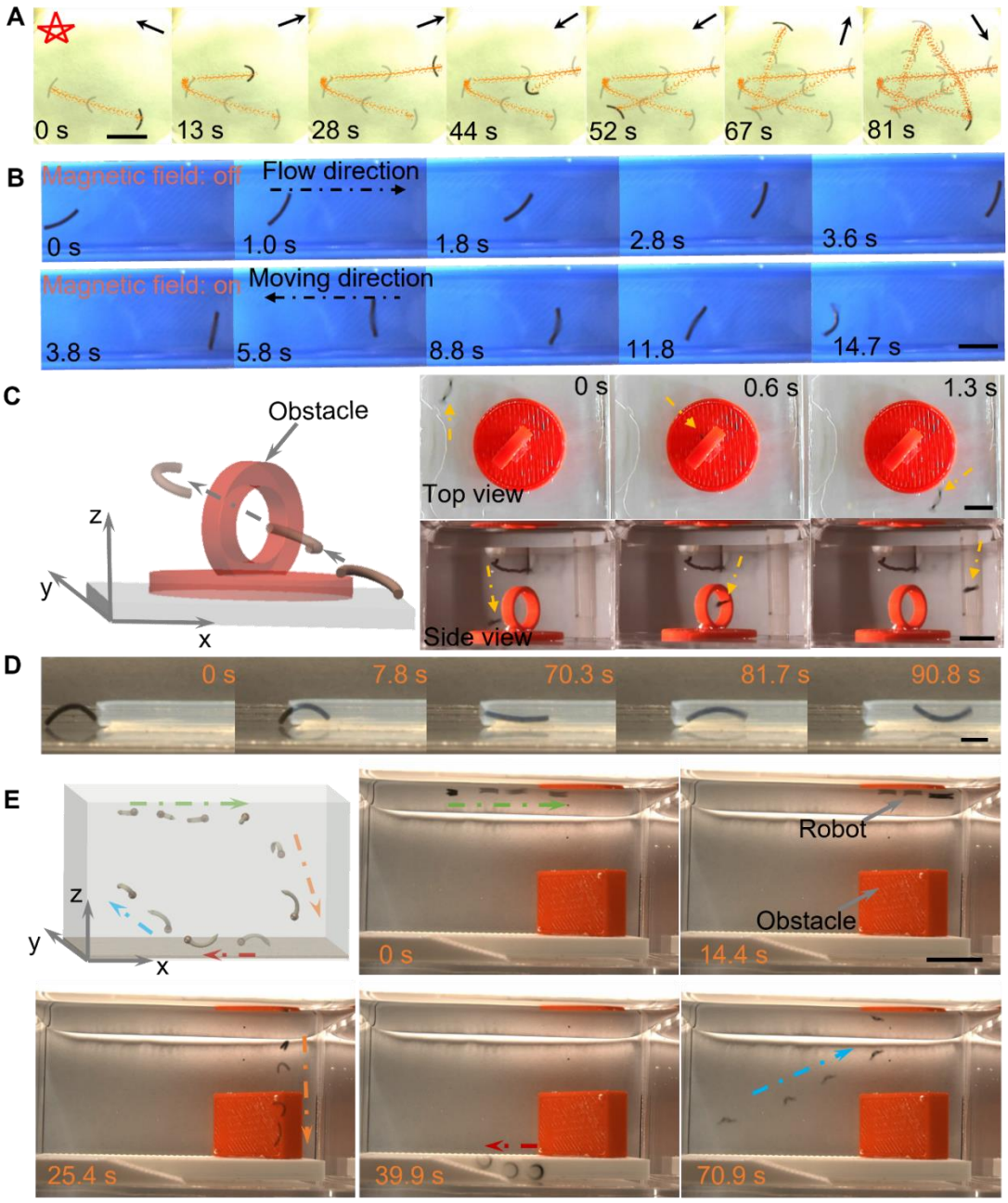

Figure 6. Multimodal locomotion of the LarvaBot. (*A*) Controllable movement of the LarvaBot along a pentagram trajectory. Arrows show the moving direction. The scale bar is 10 mm. (*B*) Propulsion of the LarvaBot in a flowing environment. The top images show the movement of the robot in the flowing environment without applying a magnetic field, and the arrow indicates the flowing direction. The bottom images show the propulsion of the robot in a flowing environment with the larva-inspired gait, and the arrow indicates the moving direction of the robot. The scale bar is 5 mm. (*C*) 3D swimming and obstacle-crossing behavior of the robot. The scale bar is 5 mm. (*D*) Crawling inside a narrow tube. The scale bar is 2 mm. (*E*) Series of multimodal locomotion including 2D swimming, immersion, rolling, and 3D swimming. The scale bar is 10 mm.

Table 1. The comparison between LarvaBot and midge larvae.

Aspects of comparison		Midge larvae	LarvaBot
Morphology	Length (mm)	2.0-29.4 (41, 48)	5
	Aspect ratio	10.4-14.3 (49, 51)	11
	Geometry	Cylindrical body	Uniform, cylindrical shape
Kinematics and dynamics	Flow regime	Intermediate flow regime (*Re* = 350, 465) (41, 51)	Intermediate flow regime (*Re* = 17-57)
	Actuation frequency (Hz)	2.66 (41)	1-4
	Motility (BL per cycle)	0.84 (41)	0.04-0.71
	Actuation method	Muscle (41)	Magnetic torque
	Wake flow pattern	Ring vortex (51)	Ring vortex
	Swimming plane	Horizontal plane (41)	Horizontal plane